Constrained Infinitesimal Dipole Modeling-Assisted Ensemble Prediction of Embedded Element Patterns via Machine Learning

Onat, Nehir Berk; Roldan, Ignacio; Fioranelli, Francesco; Yarovoy, Alexander; Aslan, Yanki

DOI
10.1109/TAP.2024.3433515

Publication date
2024

Document Version
Final published version

Published in
IEEE Transactions on Antennas and Propagation

Communication

Constrained Infinitesimal Dipole Modeling-Assisted Ensemble Prediction of Embedded Element Patterns via Machine Learning

Nehir Berk Onat, Ignacio Roldan, Francesco Fioranelli, Alexander Yarovoy, and Yanki Aslan

***Abstract*— A novel ensemble prediction technique is introduced to enhance the accuracy of far-field embedded element pattern (EEP) prediction under mutual coupling (MC) effects, while relaxing the training data size challenge in neural network (NN)-based algorithms. The proposed method integrates a two-stage NN for direct EEP prediction from full-wave simulated pattern data in spherical coordinates with a fully connected NN for the prediction of excitation coefficients of an array of infinitesimal dipoles, approximating the full-wave simulated EEPs via constrained infinitesimal dipole modeling (IDM). Quasi-randomly distributed five-element pin-fed S-band patch antenna arrays are used for demonstration purpose. It is shown that, for a large-sized (3500 topologies) and relatively small-sized (1500 topologies) dataset, incorporating IDM-NN with the benchmarked direct EEP-NN in an ensemble technique increases the pattern prediction accuracy by 11% and 60% on average, respectively.**

***Index Terms*— Aperiodic array, embedded element pattern (EEP), infinitesimal dipole modeling (IDM), machine-learning, mutual coupling (MC).**

I. Introduction

Nonuniformly spaced (aperiodic) phased array antennas promise achieving lower sidelobe levels (SLLs) at wide-angle scanning, while keeping similar or higher gain as compared to their regular counterparts [1], [2], [3]. Through array topology optimization, field-of-view specific radiation patterns can be obtained at the peak power amplifier efficiencies [4]. The optimization techniques have an iterative nature [5], [6], [7], with convergence to the lowest possible peak SLL depending on the type of the element, number of elements, aperture size, and minimal element spacing [8]. The applications include arrays for base stations [9], satellite communications [10], radio astronomy [11], and automotive radars [12].

A major challenge in aperiodic array synthesis is to take mutual coupling (MC) effects into account. Due to the complexity of estimating unique embedded element patterns (EEPs), many studies either neglect or underestimate the MC effects via stand-alone element or infinite-array assumptions [13]. This leads to unreliable results, with an unpredictable performance degradation in the physical array. A straightforward approach is to integrate full-wave simulations in the optimization routine [14], [15]. Despite its solidity, such an approach suffers from large computational requirements, while not allowing the designers to synthesize large arrays, implement what-if scenarios to test different topologies or parameters, and obtain prompt adaptive responses for layout modulation when needed.

Several analytical and numerical techniques have been proposed for modeling of MC and thus EEPs in phased arrays, such as infinite-to-finite array approach [16], an iterative technique based on the concept of multiple scattering [17], spherical-wave expansion-based technique [18], and active element pattern expansion (AEPE) [19], [20]. However, they are either computationally expensive, focused on specific element types, or not flexible enough for implementation in various topologies. More recently, machine-learning (ML)-based techniques, especially neural networks (NNs) with their ability to approximate highly nonlinear functions [21], have been successfully utilized for MC and EEP estimations in aperiodic arrays [22]. However, the proposed methods have two major limitations.

1) Data-driven ML techniques require a large amount of data to avoid overfitting, significantly increasing the computational time and load for data production.
2) There is high dependency of the result on the training data, which results in large prediction performance deviations at different array elements.

Therefore, there is a need to find a reliable method to ensure sufficiently accurate EEP prediction under different MC effects, while reducing the size of the training set.

The major contributions of this work are listed below.

1) The constrained infinitesimal dipole modeling (IDM) approach [23], [24] is used for the first time in NN training for robust pattern estimation under limited data size.
2) A novel ensemble prediction technique that combines direct pattern prediction with IDM coefficient prediction is proposed to enhance the performance of a single architecture in low-complexity NNs.
3) An optimal data-size-dependent ensembling weight is introduced for the best pattern prediction accuracy.

The rest of the communication is organized as follows. Section II introduces the antenna under test (AUT) for feasibility and IDM formulation. The proposed NN structures and ensemble prediction are presented in Section III. Section IV discusses the results. The conclusions are given in Section V.

II. Simulation Settings

A. Antenna Under Test

To demonstrate the performance of the proposed technique, five-element irregularly spaced pin-fed patch antenna elements (at 2.85 GHz center frequency) have been designed as illustrated in Fig. 1, where the main design parameters are listed in Table I. The antenna element under test for EEP prediction is placed at the origin $(0, 0)$, while the neighboring elements are randomly distributed (to create a dataset with full-wave simulations) in a defined region limited by an inner and an outer circle. The radius of the inner circle, r_1, is equal to 0.5λ, where λ is the free space wavelength at the center frequency. The radius of the outer circle $(r_1 + r_2)$ is selected as λ to observe the MC effect on the EEPs by keeping the elements close to each other. The allowed minimum distance between the elements is kept at 0.5λ, making the dataset quasi-random.

Manuscript received 19 February 2024; revised 25 June 2024; accepted 19 July 2024. Date of publication 31 July 2024; date of current version 9 September 2024. This work was supported by Delft Space Institute (DSI) Seed Grant. *(Corresponding author: Nehir Berk Onat.)*

The authors are with the Department of Microelectronics, Delft University of Technology, 2628 Delft, The Netherlands (e-mail: n.b.onat@tudelft.nl; i.roldanmontero@tudelft.nl; f.fioranelli@tudelft.nl; a.yarovoy@tudelft.nl; y.aslan@tudelft.nl).

Color versions of one or more figures in this article are available at https://doi.org/10.1109/TAP.2024.3433515.

Digital Object Identifier 10.1109/TAP.2024.3433515

TABLE I
ANTENNA DESIGN PARAMETERS

Center frequency	2.85 GHz	**Substrate length** (l_s)	0.36 mm
Patch length (l_p)	33.71 mm	**Substrate width** (w_s)	0.36 mm
Patch width (w_p)	33.71 mm	**Substrate height** (h)	1.6 mm
Circle rad. [r_1,r_2]	$[0.5, 0.3]\lambda$	**Permittivity** (ϵ_r)	2.2

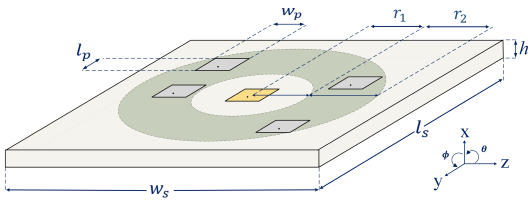

Fig. 1. Five-element aperiodic array topology where the AUT, highlighted with the yellow color, is located at the center, $(x_o, y_o) = (0, 0)$, and the neighboring elements are randomly positioned in the defined green region: $r_1^2 \leq (x_i^2 + y_i^2) \leq (r_1 + r_2)^2$ where (x_i, y_i) is the location of the ith neighbor element in λ.

B. EEP and Constrained IDM

The far-field radiation field of a phased array shown in Fig. 1 can be formulated as

$$F(\theta, \phi) = \sum_{n=1}^{N=5} w_n E_n(\theta, \phi)\, e^{jk(y_n \sin\theta \sin\phi + z_n \cos\theta)} \quad (1)$$

where w_n is the weight and $E_n(\theta, \phi)$ is the EEP of the nth element, k is the wavenumber, and y_n and z_n are the positions of the nth element in y- and z-axis, respectively.

Estimating $E_n(\theta, \phi)$ for any given topology fast and accurately will allow synthesizing the desired $F(\theta, \phi)$ (e.g., for pattern shaping or pattern nulling) reliably. In ML-assisted estimations of $E_n(\theta, \phi)$, the EEPs of each AUT in the training dataset can be simulated via full-wave commercial software. Then, NN can be trained on the pattern data on spherical coordinates [25]. Alternatively, the EEPs can be efficiently approximated by using the constrained IDM where the original array surface is populated with an equivalent array of infinitesimal electric, $e-$ and magnetic, $m-$dipoles [26]. The excitation coefficients of the dipoles can be estimated via inversion of a Vandermonde-type matrix [27], which is relaxed by introducing a relatively small Gaussian noise [28], [29]. Although using both dipole types along the y- and z-axes in a dense ID array provides a more accurate approximation of the pattern, the inversion of a matrix with a high condition number makes the ID coefficients very sensitive against errors. Improving robustness is critical as it is expected that NN predictions introduce errors in the ID coefficients. In [30], it was shown that the best condition number versus pattern approximation error trade-off is achieved when only $m-$dipoles oriented along the radiating edges of a patch, i.e., along the z-axis, are used on a sunflower ID array layout. In particular, for a maximal array radius of λ as in Fig. 1, the use of 81 dipoles was motivated as the optimal ID array size [30]. This preliminary study is exploited in this communication in IDM formulation for NN-based EEP prediction.

III. PROPOSED METHODOLOGIES

In this section, two different methods for estimating the absolute EEPs are presented. Both of them use as input the coordinates of the four elements placed in the ring in Fig. 1. The first (benchmarked) method directly estimates the center element's EEP including the neighbor elements' effect. On the other hand, the second and novel method estimates the ID coefficients, and with this, IDM is applied to obtain the EEP. Moreover, both methods are combined in an innovative ensemble model to generate better predictions than each of them alone. Fig. 2 shows a block diagram of the full pipeline, highlighting in blue the direct EEP prediction, in green the IDM prediction, and in yellow the ensemble model.

In Sections III-A–III-C, each block is explained in detail.

A. Direct NN EEP Prediction

A NN inspired by the one presented in [25] has been designed to predict the central element's EEP directly in the θ-ϕ domain. The NN consists of two different parts; the first one generates a low-resolution EEP of 36×36, while the second part upscales it to the desired resolution of 180×180 (1° resolution in azimuth and elevation). In contrast with the method presented in [25], both blocks are trained together, and therefore, the intermediate low-resolution result is not provided. The upscale block is based on the efficient subpixel convolutional NN (ESPCN) [31]. A schematic of the proposed architecture can be seen in the blue part of Fig. 2.

The input to the proposed network $P \in \mathbb{R}^{4\times 2}$ contains the position in polar coordinates of the elements, and it is fed to a 1-D convolutional layer with 16 kernels, which encodes the spatial relationships. Then, seven fully connected layers are used, increasing the number of neurons in each step until it reaches 1296. The number of layers and neurons have been tuned manually following a heuristic search [32]. The output of the fully connected layers is then reshaped from 1296 into a 36×36 matrix resembling a low-resolution EEP. Finally, the ESPCN architecture is used to upscale it to a 180×180 matrix. This architecture uses two convolutional layers for feature map extraction and a subpixel convolution layer that aggregates the feature maps from the low-resolution space and builds the high-resolution image. In this work, the two hidden convolutional layers have n=32 filters and 3×3 kernel size, while the subpixel layer has r2=25 filters to achieve five times the input resolution (upscaling from 36×36 to 180×180). The whole NN model is composed of 2 million parameters, which is a small number for NN architectures [33], with an estimation time several orders of magnitude faster than full-wave simulations [25].

The key to a successful estimation of the EEP is the use of the structural similarity (SSIM) index as a loss for training the NN. The SSIM was originally developed as a metric for measuring image quality given a reference image, usually to assess the losses due to image compression. However, it has been used recently as a loss function for training NNs [34]. Formally, the SSIM is defined per pixel as

$$\text{SSIM}(\text{p}) = \frac{2\mu_x\mu_y + C_1}{\mu_x^2 + \mu_y^2 + C_1} \cdot \frac{2\sigma_{xy} + C_2}{\sigma_x^2 + \sigma_y^2 + C_2} \quad (2)$$

where as follows.

1) The means μ and standard deviations σ are computed with an 11×11 Gaussian filter of width 1.5.
2) $C_1 = (k_1 L)^2$, $C_2 = (k_2 L)^2$, are two constants.
3) L is the dynamic range of the matrix (i.e., the difference between the maximum and minimum value).
4) k_1 and k_2 are set to the default values of 0.01 and 0.03.

Then, the loss for each matrix can be defined as

$$\mathcal{L}^{\text{SSIM}}(\text{P}) = 1 - \frac{1}{N} \sum_{p \in P} \text{SSIM}(\text{p}). \quad (3)$$

The use of the SSIM loss is a critical component of this work since the value of each matrix element in the EEP is strongly correlated with its neighbors. The SSIM enforces this structural information,

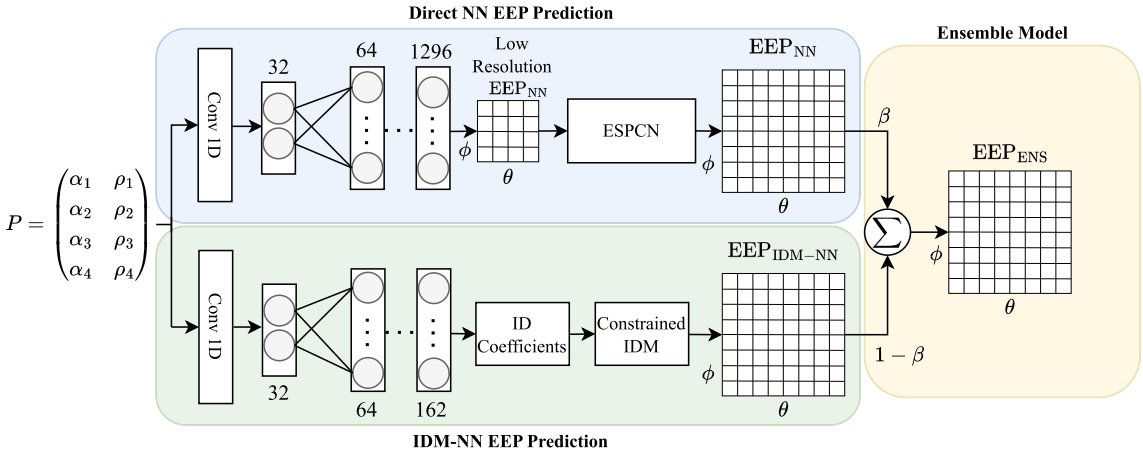

Fig. 2. Block diagram of the proposed method. The upper branch (in blue) directly predicts the EEP using a two-stage network based on the previous study [25] and the ESPCN [31] architecture. The lower branch (in green) uses a NN to estimate the ID complex coefficients, and then the constrained IDM generates the EEP. Finally, the ensemble model (in yellow) combines both predictions to generate a higher quality estimation.

in contrast with minimum squared error (MSE) or mean absolute error (MAE) which are computed per cell independently.

B. IDM-NN EEP Prediction

A schematic of the network is presented in Fig. 2 highlighted in green. The second approach aims to estimate the 81 $z-$oriented $m-$type IDs complex excitations coefficients for given element positions. In this case, the estimation space is much smaller (81 complex coefficients versus 32 400); therefore, a simpler network has been used. Similarly, the first layer is a 1-D convolutional layer with 16 kernels to encode the spatial information. Then, in order to maintain the same number of layers as in the previous architecture (to have the same network depth and fair comparison of results), seven fully connected layers are included with a final output vector of dimension 81×2 (real and imaginary parts).

The network is trained using the ADAM optimizer [35] with the default hyperparameters (η=0.001, β_1=0.9, β_2=0.999, ϵ=1e-7) and the MSE between the estimated and the true ID coefficients as loss function. Once the ID coefficients are predicted, the EEP can be estimated using the IDM technique explained in Section II-B.

C. Ensemble Model

A common practice to tackle difficult tasks in ML is to use the prediction of different models and combine the output to obtain better performance of any of the models alone. This is known as ensemble models, and this technique is used to overcome the limitations that each of the proposed methods presents. Moreover, this allows the design of low-complexity NN architectures suitable for problems when the number of training data is limited. Although several tools can be utilized to obtain an ensemble model, this study employs a simple pixel-wise weighted sum to show the potential of the ensemble prediction with the proposed methods, as illustrated in Fig. 2 highlighted in yellow.

IV. Results

Defining the cost function is a critical task due to the high difference between the minimum and maximum values of the EEP, causing a challenge in quantifying the prediction error. In this study, the error is computed for the region $45° \leq \theta \leq 135°$ and $-45° \leq \phi \leq 45°$ which describes the angular region of interest for the typical array

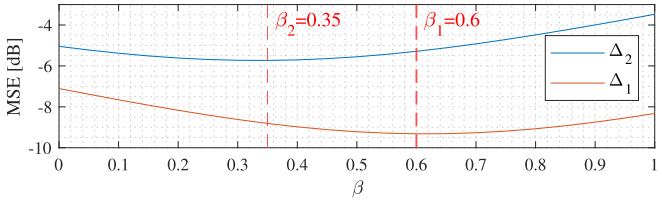

Fig. 3. Analysis of the weighting value, β, for the ensemble prediction where Δ_1 and Δ_2 represent the datasets comprising 3500 and 1500 data, respectively. The MSE of each point is calculated over the validation set where $\beta_1 = 0.6$ and $\beta_2 = 0.35$ provide the minimum error for the datasets Δ_1 and Δ_2, respectively.

applications, comprising the high gain part of the EEP. Therefore, the absolute level of the resulting error is naturally expected to be high regardless of the chosen error function. To this extent, a commonly used error function, the MSE, has been selected to quantify the error between the full-wave simulated and predicted EEPs

$$\varepsilon_p = 10 \lg \left(\frac{1}{N_s^2} \sum_{i,j=1}^{N_s} \left(|EEP_{\text{CST}}(\theta_i, \phi_j)| - |EEP'_p(\theta_i, \phi_j)| \right)^2 \right) \tag{4}$$

where N_s is the number of samples for θ and ϕ, EEP_{CST} is the full-wave simulated pattern of the chosen element in the far-field region that is generated by the commercial full-wave simulator CST, EEP'_p, and ε_p are the corresponding predicted pattern and its MSE with p indicating the used methodology.

Two different-sized datasets with quasi-randomly generated 1500 and 3500 full-wave simulations by CST, where each data comprise an EEP of an AUT with 180-by-180 samples (in terms of E-field magnitudes in dB), were used for the training of the NNs. These two datasets were chosen based on the average error analysis, whereas reducing the dataset below 1500 data increases the error significantly (larger than -3.7 dB), while error remains relatively low (below -9.2 dB) beyond 3500 data for the considered topology. Among these data, 300 of them were chosen as a validation for both sets.

The results are presented for five different EEP methodologies, which demonstrates the potential of the proposed ensemble prediction. These methodologies include: 1) full-wave simulated isolated

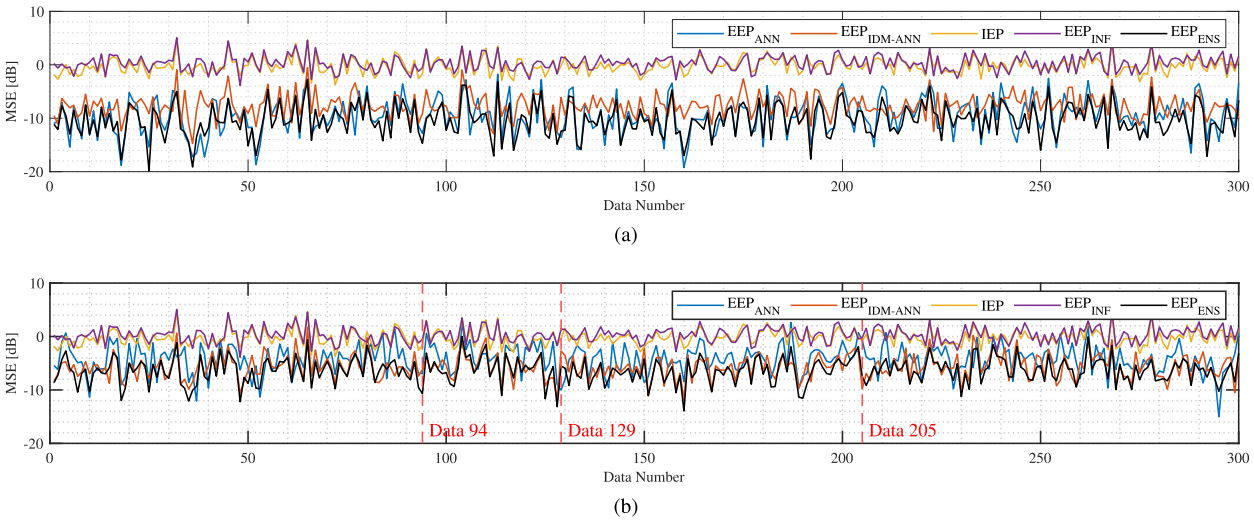

Fig. 4. MSE comparison for the validation set with two different training data sizes. (a) $\Delta_1 = 3500$ training data and (b) $\Delta_2 = 1500$ training data.

TABLE II

RESULTS FOR EACH CASE STUDY AND THE AVERAGE OVER THE VALIDATION SETS WITH THE BENCHMARK PATTERNS

Error (MSE)	Avg. 1	Avg. 2	Case 1	Case 2	Case 3
$\varepsilon_{\mathrm{IEP}}$ [dB]	0.10	0.07	-0.23	-0.85	-1.73
$\varepsilon_{\mathrm{UNT}}$ [dB]	0.60	0.55	1.43	-0.18	-0.56
$\varepsilon_{\mathrm{NN}}$ [dB]	-8.30	-3.48	-10.03	-0.67	-12.80
$\varepsilon_{\mathrm{IDM-NN}}$ [dB]	-7.10	-5.04	-2.69	-9.83	-9.14
$\varepsilon_{\mathrm{ENS}}$ [dB]	-9.32	-5.73	-5.53	-7.51	-14.10

Notes: Avg. 1 and Avg. 2 indicate the average MSE of the networks trained with the datasets Δ_1 and Δ_2 over the same validation set, whereas the cases are trained with the dataset Δ_2. Case 1, 2, and 3 correspond to the data numbers 129, 205, and 94, respectively.

element pattern (IEP); 2) full-wave simulated unit cell element pattern in an infinite array ($\mathrm{EEP_{UNT}}$); 3) direct ANN predicted EEP ($\mathrm{EEP_{ANN}}$); 4) IDM-ANN predicted EEP ($\mathrm{EEP_{IDM-ANN}}$); and 5) ensemble-predicted EEP ($\mathrm{EEP_{ENS}}$).

The weighting factor, β, is analyzed to obtain an optimum choice for the ensemble prediction block for each training set. Fig. 3 illustrates the MSE results for each β value for the datasets Δ_1, comprising 3500 training data, and Δ_2, comprising 1500 training data. The cost function MSE is calculated over the same validation set. While the minimum error is obtained by $\beta = 0.35$ for the network trained with the dataset Δ_2, the value of the weight factor shifts to 0.6 with the increase of the training data as shown in Fig. 3. It is possible to use ensemble learning techniques to learn the best β for each situation, which is left out of the scope of this work and will be considered in future work.

First, each model is trained with the large dataset, Δ_1, and the corresponding results are illustrated in Fig. 4(a) for each validation data, and Table II shows the average results. While the MSE of the IEP and $\mathrm{EEP_{UNT}}$ has an average of 0.3 dB, the NN-direct predicted element pattern $\mathrm{EEP'_{NN}}$ and the IDM-NN predicted element pattern $\mathrm{EEP'_{IDM-NN}}$ have an average error of -8.3 and -7.1 dB, respectively. Although the MSE of the ANN-based methods generally remains low, the error in specific topology cases can be observed to be higher than the others. These high errors are reduced by the proposed ensemble prediction where the error in $\mathrm{EEP'_{ENS}}$ has an average MSE of -9.3 dB over the validation set.

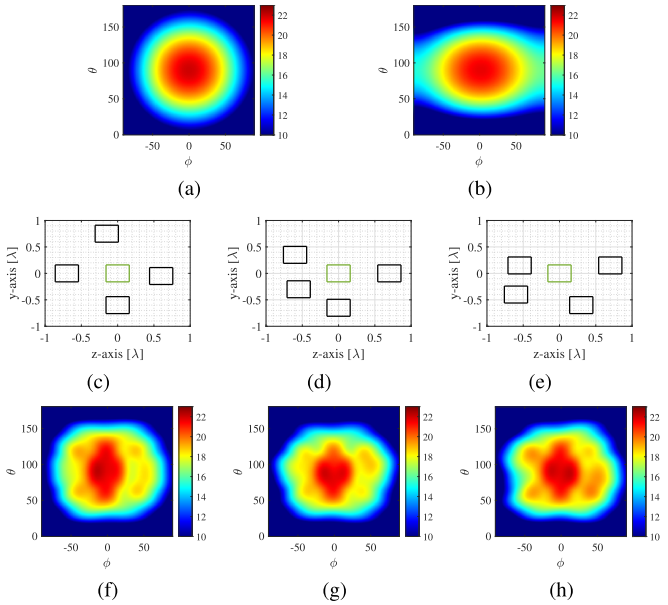

Fig. 5. Five-element array topologies with different case studies with the corresponding EEPs (E-field, in dB) where the MC effect can easily be observed. The green and black rectangles in the topology figures illustrate the main and neighbor elements, respectively. (a) IEP, (b) $\mathrm{EEP_{UNT}}$, (c) topology of Data 129, (d) topology of Data 205, (e) topology of Data 94, (f) $\mathrm{EEP_{CST}}$ of Data 129, (g) $\mathrm{EEP_{CST}}$ of Data 205, and (h) $\mathrm{EEP_{CST}}$ of Data 94.

When the size of the dataset is reduced by almost 60% to 1500 data, the prediction performance of the NN-based methods becomes worse. Yet, the performance of the proposed ensemble methodology remains in the acceptable range, as can be seen in Fig. 4(b) and Table II. To illustrate the performance of the trained networks visually and to highlight the benefits of ensemble prediction, three extreme cases, namely Data 129, 205, and 94, have been selected from the validation set as visualized in Fig. 4(b). The topologies of these cases are illustrated in Fig. 5 with the full-wave simulated AUT pattern ($\mathrm{EEP_{CST}}$) where the MC effect on the EEPs can easily be observed as compared to the IEP and $\mathrm{EEP_{UNT}}$. A summary of the average error result comparisons for the three cases is also provided in Table II for completeness.

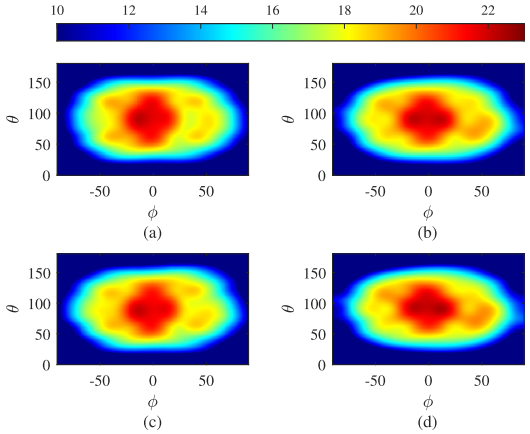

Fig. 6. Case 1: EEP (E-field, in dB) prediction results for Data 129 with the training set Δ_2. (a) EEP_{CST} is full-wave simulated EEP, (b) EEP_{ENS} is the ensemble predicted EEP, (c) EEP_{NN} is the direct NN predicted EEP, and (d) $\text{EEP}_{\text{IDM}-\text{NN}}$ is the IDM-NN predicted EEP.

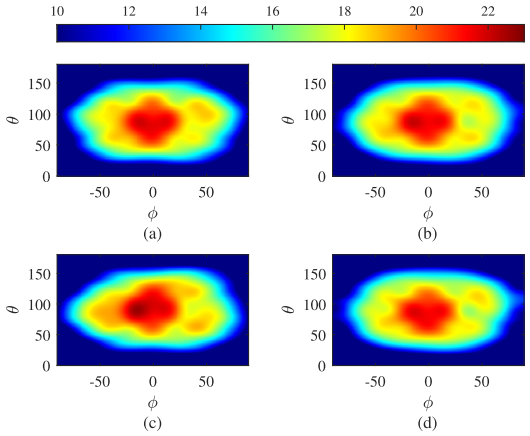

Fig. 7. Case 2: EEP (E-field, in dB) prediction results for Data 205 with the training set Δ_2. (a) EEP_{CST} is full-wave simulated EEP, (b) EEP_{ENS} is the ensemble predicted EEP, (c) EEP_{NN} is the direct NN predicted EEP, and (d) $\text{EEP}_{\text{IDM}-\text{NN}}$ is the IDM-NN predicted EEP.

A. Topology Case 1

In the first example in Fig. 6, while both models provide the outline of the full-wave simulated pattern of the AUT, IDM-NN model fails to predict particularly main beam region and corner regions (e.g., $-60^\circ < \phi < -25^\circ$ and $30^\circ < \theta < 70^\circ$) as can be observed in Fig. 6(c). Errors in these regions are suppressed by the prediction of the NN-direct model as a result of the ensemble prediction that is shown in Fig. 6(b). In this way, the MSE between the full-wave simulated pattern and prediction is reduced from -2.69 to -5.53 dB.

B. Topology Case 2

In a case like this, the NN methodology suffers from a higher prediction error, while the IDM-NN model provides a better prediction, as seen in Fig. 7. In this example, the error by the NN-direct prediction is reduced from -0.67 to -7.51 dB by the superior prediction by the IDM-NN model, as can be seen in Table II.

C. Topology Case 3

In rare cases, the error of both predictions can be relatively low, as shown in Fig. 4(b). Particularly in these cases, the ensemble prediction reduces and stabilizes the peak errors even more by averaging the resulting patterns from the proposed ANN methodologies. Even with a simple averaging, the obtained ensemble prediction agrees with the full-wave simulation by decreasing the error from -9.14 to -14.1 dB as visually illustrated in Fig. 8.

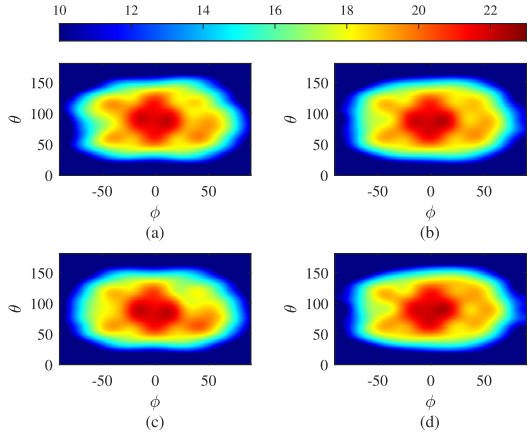

Fig. 8. Case 3: EEP (E-field, in dB) prediction results for Data 94 with the training set Δ_2. (a) EEP_{CST} is full-wave simulated EEP, (b) EEP_{ENS} is the ensemble predicted EEP, (c) EEP_{NN} is the direct NN predicted EEP, and (d) $\text{EEP}_{\text{IDM}-\text{NN}}$ is the IDM-NN predicted EEP.

V. Conclusion

A novel ensemble prediction technique is proposed to achieve sufficiently accurate and fast EEP prediction under different MC effects with reduced training data size. The method is based on combining: 1) a direct approach comprising a two-stage NN that predicts EEPs in $\theta - \phi$ plane from the full-wave simulated data and 2) the constrained IDM, where ID excitations are predicted by a second NN, obtaining the EEP from the predicted coefficients. For validation, quasi-random five-element S-band pin-fed patch array topologies are employed. The results have proven the potential of the proposed method in achieving a lower MSE in EEPs (by about 60% on average) while reducing the data size (by nearly 60%). Future work will explore more advanced NN architectures and the training of the full ensembling model as a single structure. Additionally, to improve the accuracy of the datasets toward the real products, future work might also consider introducing realistic parameter sensitivity-error models in the simulations.

References

[1] O. M. Bucci, M. D'Urso, T. Isernia, P. Angeletti, and G. Toso, "Deterministic synthesis of uniform amplitude sparse arrays via new density taper techniques," *IEEE Trans. Antennas Propag.*, vol. 58, no. 6, pp. 1949–1958, Jun. 2010.

[2] D. Pinchera, M. D. Migliore, and G. Panariello, "Synthesis of large sparse arrays using IDEA (inflating-deflating exploration algorithm)," *IEEE Trans. Antennas Propag.*, vol. 66, no. 9, pp. 4658–4668, Sep. 2018.

[3] Y. Aslan, A. Roederer, and A. Yarovoy, "System advantages of using large-scale aperiodic array topologies in future mm-wave 5G/6G base stations: An interdisciplinary look," *IEEE Syst. J.*, vol. 16, no. 1, pp. 1239–1248, Mar. 2022.

[4] J. L. A. Quijano, M. Righero, and G. Vecchi, "Sparse 2-D array placement for arbitrary pattern mask and with excitation constraints: A simple deterministic approach," *IEEE Trans. Antennas Propag.*, vol. 62, no. 4, pp. 1652–1662, Apr. 2014.

[5] D. G. Kurup, M. Himdi, and A. Rydberg, "Synthesis of uniform amplitude unequally spaced antenna arrays using the differential evolution algorithm," *IEEE Trans. Antennas Propag.*, vol. 51, no. 9, pp. 2210–2217, Sep. 2003.

[6] L. Cen, Z. L. Yu, W. Ser, and W. Cen, "Linear aperiodic array synthesis using an improved genetic algorithm," *IEEE Trans. Antennas Propag.*, vol. 60, no. 2, pp. 895–902, Feb. 2012.

[7] B. Fuchs, A. Skrivervik, and J. R. Mosig, "Synthesis of uniform amplitude focused beam arrays," *IEEE Antennas Wireless Propag. Lett.*, vol. 11, pp. 1178–1181, 2012.

[8] Y. Aslan, J. Puskely, A. Roederer, and A. Yarovoy, "Multiple beam synthesis of passively cooled 5G planar arrays using convex optimization," *IEEE Trans. Antennas Propag.*, vol. 68, no. 5, pp. 3557–3566, May 2020.

[9] X. Ge, R. Zi, H. Wang, J. Zhang, and M. Jo, "Multi-user massive MIMO communication systems based on irregular antenna arrays," *IEEE Trans. Wireless Commun.*, vol. 15, no. 8, pp. 5287–5301, Aug. 2016.

[10] C. Bencivenni, M. V. Ivashina, R. Maaskant, and J. Wettergren, "Synthesis of maximally sparse arrays using compressive sensing and full-wave analysis for global Earth coverage applications," *IEEE Trans. Antennas Propag.*, vol. 64, no. 11, pp. 4872–4877, Nov. 2016.

[11] W. V. Cappellen, S. Wijnholds, and J. Bregman, "Sparse antenna array configurations in large aperture synthesis radio telescopes," in *Proc. EuRAD*, 2006, pp. 76–79.

[12] D. Mateos-Nunez, M. A. Gonzalez-Huici, R. Simoni, F. B. Khalid, M. Eschbaumer, and A. Roger, "Sparse array design for automotive MIMO radar," in *Proc. 16th Eur. Radar Conf. (EuRAD)*, Oct. 2019, pp. 249–252.

[13] H. Singh, H. L. Sneha, and R. M. Jha, "Mutual coupling in phased arrays: A review," *Int. J. Antennas Propag.*, vol. 2013, no. 1, 2013, Art. no. 348123.

[14] C. Bencivenni, M. V. Ivashina, R. Maaskant, and J. Wettergren, "Design of maximally sparse antenna arrays in the presence of mutual coupling," *IEEE Antennas Wireless Propag. Lett.*, vol. 14, pp. 159–162, 2015.

[15] Y. Aslan, M. Candotti, and A. Yarovoy, "Synthesis of multi-beam space-tapered linear arrays with side lobe level minimization in the presence of mutual coupling," in *Proc. 13th Eur. Conf. Antennas Propag. (EuCAP)*, Mar. 2019, pp. 1–5.

[16] J. I. Echeveste, M. Á. G. de Aza, J. Rubio, and C. Craeye, "Gradient-based aperiodic array synthesis of real arrays with uniform amplitude excitation including mutual coupling," *IEEE Trans. Antennas Propag.*, vol. 65, no. 2, pp. 541–551, Feb. 2017.

[17] T. Marinovic et al., "Fast characterization of mutually coupled array antennas using isolated antenna far-field data," *IEEE Trans. Antennas Propag.*, vol. 69, no. 1, pp. 206–218, Jan. 2021.

[18] J. Corcoles, J. Rubio, and M. Á. Gonzalez, "Spherical-wave-based shaped-beam field synthesis for planar arrays including the mutual coupling effects," *IEEE Trans. Antennas Propag.*, vol. 59, no. 8, pp. 2872–2881, Aug. 2011.

[19] P. You, Y. Liu, X. Huang, L. Zhang, and Q. H. Liu, "Efficient phase-only linear array synthesis including coupling effect by GA-FFT based on least-square active element pattern expansion method," *Electron. Lett.*, vol. 51, no. 10, pp. 791–792, May 2015.

[20] X. Huang, Y. Liu, P. You, M. Zhang, and Q. H. Liu, "Fast linear array synthesis including coupling effects utilizing iterative FFT via least-squares active element pattern expansion," *IEEE Antennas Wireless Propag. Lett.*, vol. 16, pp. 804–807, 2017.

[21] A. Massa, D. Marcantonio, X. Chen, M. Li, and M. Salucci, "DNNs as applied to electromagnetics, antennas, and propagation—A review," *IEEE Antennas Wireless Propag. Lett.*, vol. 18, pp. 2225–2229, 2019.

[22] C. Cui, W. T. Li, X. T. Ye, Y. Q. Hei, P. Rocca, and X. W. Shi, "Synthesis of mask-constrained pattern-reconfigurable nonuniformly spaced linear arrays using artificial neural networks," *IEEE Trans. Antennas Propag.*, vol. 70, no. 6, pp. 4355–4368, Jun. 2022.

[23] M. Serhir, P. Besnier, and M. Drissi, "An accurate equivalent behavioral model of antenna radiation using a mode-matching technique based on spherical near field measurements," *IEEE Trans. Antennas Propag.*, vol. 56, no. 1, pp. 48–57, Jan. 2008.

[24] M. Serhir, P. Besnier, N. Ribiere-Tharaud, and M. Drissi, "The use of infinitesimal dipoles and the spherical wave expansion for planar antennas modeling," in *Proc. 4th Eur. Conf. Antennas Propag.*, Apr. 2010, pp. 1–5.

[25] N. B. Onat, I. Roldan, F. Fioranelli, A. Yarovoy, and Y. Aslan, "Efficient embedded element pattern prediction via machine learning: A case study with planar non-uniform sub-arrays," in *Proc. 17th Eur. Conf. Antennas Propag. (EuCAP)*, Mar. 2023, pp. 1–5.

[26] S. J. Yang, Y. D. Kim, D. J. Yun, D. W. Yi, and N. H. Myung, "Antenna modeling using sparse infinitesimal dipoles based on recursive convex optimization," *IEEE Antennas Wireless Propag. Lett.*, vol. 17, pp. 662–665, 2018.

[27] L. R. Turner, "Inverse of the Vandermonde matrix with applications," NASA, Washington, DC, USA, Tech. Rep. NASA-TN-D-3547, 3547.

[28] V. H. Vu and T. Tao, "The condition number of a randomly perturbed matrix," in *Proc. 39th Annu. ACM Symp. Theory Comput.*, Jun. 2007, pp. 248–255.

[29] H. G. Moura, E. C. Junior, A. Lenzi, and V. C. Rispoli, "On a stochastic regularization technique for ill-conditioned linear systems," *Open Eng.*, vol. 9, no. 1, pp. 52–60, Feb. 2019.

[30] N. B. Onat, A. Yarovoy, and Y. Aslan, "Sunflower array of infinitesimal dipoles for constrained antenna modeling," in *Proc. 18th Eur. Conf. Antennas Propag. (EuCAP)*, Mar. 2024, pp. 1–5.

[31] W. Shi et al., "Real-time single image and video super-resolution using an efficient sub-pixel convolutional neural network," in *Proc. IEEE Conf. Comput. Vis. Pattern Recognit. (CVPR)*, Jun. 2016, pp. 1874–1883.

[32] D. Stathakis, "How many hidden layers and nodes?" *Int. J. Remote Sens.*, vol. 30, no. 8, pp. 2133–2147, Apr. 2009.

[33] X. Xu et al., "Scaling for edge inference of deep neural networks," *Nature Electron.*, vol. 1, no. 4, pp. 216–222, Apr. 2018.

[34] H. Zhao, O. Gallo, I. Frosio, and J. Kautz, "Loss functions for image restoration with neural networks," *IEEE Trans. Comput. Imag.*, vol. 3, no. 1, pp. 47–57, Mar. 2017.

[35] D. Kingma and J. Ba, "Adam: A method for stochastic optimization," in *Proc. ICLR*, 2014, p. 1.